Strength anisotropy of shales deformed under uppermost crustal conditions

Audrey Bonnelye

Alexandre Schubnel

Christian David

Pierre Henry

Yves Guglielmi

Claude Gout
Anne-Laure Fauchille

Pierre Dick
First published: 29 September 2016

https://doi.org/10.1002/2016JB013040

Cited by: 5
UC-eLinks
This article is a companion to *Bonnelye et al.* [2017] doi: 10.1002/2016JB013540.
SECTIONS

PDF
TOOLS

SHARE

Abstract

Conventional triaxial tests were performed on three sets of samples of Tournemire shale along different orientations relative to bedding (0°, 45°, and 90°). Experiments were carried out up to failure at increasing confining pressures ranging from 2.5 to 160 MPa, at strain rates ranging between $3 \times 10^{-7}s^{-1}$ and $3 \times 10^{-5}s^{-1}$. This allowed us to determine the entire anisotropic elastic compliance matrix as a function of confining pressure. Results show that the orientation of principal stress relative to bedding plays an important role on the brittle strength, with 45° orientation being the weakest. We fit our results with a wing crack micromechanical model and an anisotropic fracture toughness. We found low values of internal friction coefficient and apparent friction coefficient in agreement with friction coefficient of clay minerals (between 0.2 and 0.3) and values of K_{Ic} comparable to that already published in the literature. We also showed

that strain rate has a strong impact on peak stress and that dilatancy appears right before failure and hence highlighting the importance of plasticity mechanisms. Although brittle failure was systematically observed, stress drops and associated slips were slow and deformation always remained aseismic (no acoustic emission were detected). This confirms that shales are good lithological candidates for shallow crust aseismic creep and slow slip events.

1 Introduction

Clayrocks or shales constitute a large portion of basin sedimentary rocks [*Hornby et al.*, 1994], accretionary wedges [*Yamaguchi et al.*, 2011; *Chester et al.*, 2013], and the uppermost part of active fault zones [*Solum et al.*, 2006; *Hirono et al.*, 2014; *Li et al.*, 2013]. The strength, fluid transport, and elastic properties of shales thus play a crucial role on faults hydromechanical behavior [*Rice*, 1992; *Faulkner et al.*, 2011]. The hydromechanical behavior of shales is also of major interest in the petroleum industry, for fluid migration understanding during production, and because shales constitute the cap rock of most reservoirs [*Gale et al.*, 2014]. In addition, because of their low permeability and swelling properties, shales have been considered as potential host rocks for nuclear waste long-term storage in several countries and studies on clayrocks are being carried out in deep underground laboratories (Tournemire for IRSN (French Institute for Nuclear Safety), Bure for ANDRA (French Agency for Nuclear Waste Management), and Mont-Terri in Switzerland). For all these reasons, laboratory investigations of physical and hydromechanical properties of shales under in situ pressure and temperature conditions are needed.

Shales are complex polymineralic materials that have a strong anisotropy due to the superposition of several causes [*Horne*, 2013; *Bandyopadhyay*, 2009]: the sedimentary nature of this rock, which is constituted of a stack of thin layers, with tight porosity made of nanometric to micrometric cracks and nonspherical pores located between those layers, and finally, the platelet shape of clay minerals [*Ulm and Abousleiman*, 2006]. In consequence, shales exhibit a strong anisotropy in both physical and mechanical properties, which has been observed both at the field scale [*Alkhalifah and Rampton*, 2001; *Le Gonidec et al.*, 2012] and the laboratory scale [*Ibanez and Kronenberg*, 1993; *Masri et al.*, 2014; *Ikari et al.*, 2015]. In particular, several experimental studies investigated the anisotropic strength of shales [*Niandou et al.*, 1997; *Dewhurst et al.*, 2015; *Shea and Kronenberg*, 1993]. Including studies performed on other anisotropic rocks such as slates, mica schists, and gneiss [*Shea and Kronenberg*, 1992, 1993; *Rawling et al.*, 2002], models of anisotropic failure criterions, either semiempirical [*Kronenberg et al.*, 1990; *Cazacu and Cristescu*, 1999; *Tien and Kuo*, 2001] or micromechanical [*Rawling et al.*, 2002], have been developed.

Our study aims at understanding the interplay between brittle and plastic mechanisms in an anisotropic material and how this is affected by strain rate. In that regard, investigating concurrently deformation, strength, and elastic wave velocities, all known to be sensitive—at a different scale—to crack formation and damage, may help to understand the active micromechanisms involved during deformation. Here a set of triaxial tests was performed under uppermost crustal in situ pressure conditions (0–160 MPa confining pressure), on Tournemire shale samples coming from three boreholes drilled along different orientations—parallel, perpendicular, and at 45°—relative to the stratification plane. Stress, strains, and elastic wave velocities were measured continuously during deformation experiments performed at two different strain rates ($\sim 10^{-7} s^{-1}$ and $\sim 10^{-5} s^{-1}$). In this paper, we focus on the stress-strain data set, which provides information about the deformation at the macroscopic scale (sample size) and we discuss failure criterion anisotropy. A companion paper [*Bonnelye et al.*, 2017] focusing on the evolution of elastic wave velocities during deformation provides additional information on the respective role played by cracking and plasticity (mineral reorientation), at the microscopic scale. In both cases, postmortem microstructural observations of deformed samples support our observations.

2 Experimental Methods

2.1 Sample Characterization and Preparation

Tournemire shale comes from the experimental underground laboratory of the Institut de Radioprotection et Sureté Nucléaire (IRSN) located in Tournemire (southern France). The tunnel is located within a Toarcian layer, deposited during marine transgression in a north-south Permian-Mesozoic basin. A detailed description of the geological context can be found in *Constantin et al.* [2004].

Three boreholes were drilled with the selected orientations (0°, 45°, and 90° with respect to bedding), in one of the galleries of the underground laboratory (they are distant of no more than 5 m from each other), in a relatively nonfractured zone. In the following, the three sets of samples will be referred to by their orientation: ϕ = 0°, 45°, and 90°, where ϕ is defined as the angle between the core sample axis and the bedding plane (Figure 1). The boreholes were dry drilled (using air as cooling fluid) by IRSN, directly at a diameter of 42 mm, and dry cut at a length ∼10 cm in the tunnel. In order to prevent our samples from desaturation, they were vacuum packed right after drilling and until being prepared for the mechanical experiments.

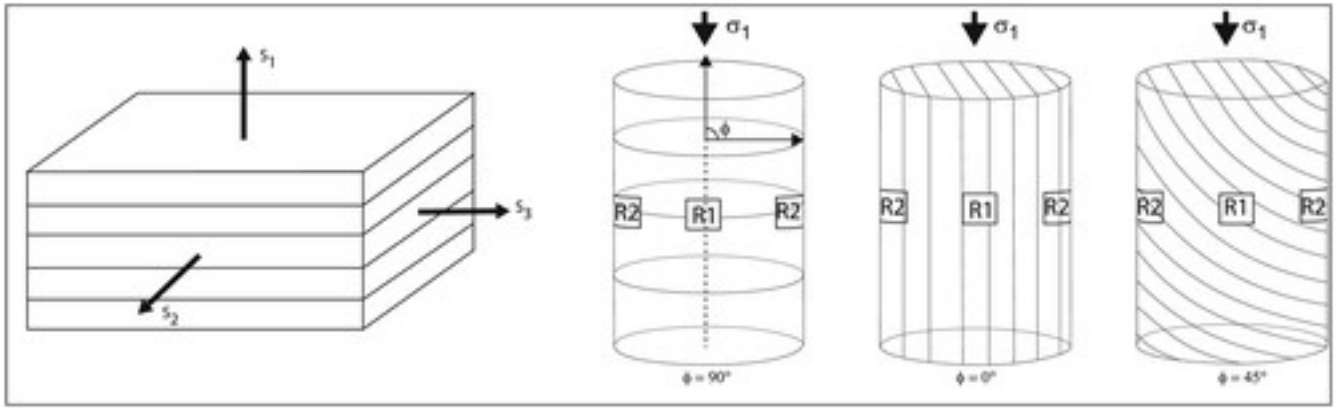

Figure 1

Open in figure viewerPowerPoint

Coordinate system used to define the compliance matrix and tangent moduli. Sample configurations with angle ϕ definition and strain gages location for each bedding orientation. Note that on each strain gage location, there is one axial and one radial strain gage.

The average mineralogical composition of Tournemire shale is detailed in Table 1 [*Tremosa et al.*, 2012]. We note the presence of an important amount of swelling clay minerals such as illite and smectite. Due to their sedimentary nature, the mineralogy percentages can exhibit a wide range of values. Most previous studies show that the variations of both physical properties and mineralogical composition seem to be mostly linked to fractured zones and/or fluid circulation. As we selected a nonfractured zone to take our samples and because the boreholes used for sampling were close to one another, the sample variability is minimized. Moreover, we consider our samples as individually homogenous as the characteristic length of default (bedding planes in our case) is small compared to the sample size.

Table 1. Range of Mineral Composition of Tournemire Shale [From *Tremosa et al.*, 2012]

Quartz (%)	10 to 20
Calcite (%)	10 to 20
Illite (%)	15 to 25
Kaolinite (%)	15 to 25

I/S (%)	15 to 20

Moreover, in order to control the heterogeneity of our specimens, characterization tests were performed both in the field and in the laboratory. First, saturation and density measurements were done on adjacent samples directly in the underground laboratory, with the protocol described in *Matray et al.* [2007], right after the drilling. The results are presented in Figure 2. From these measurements, we see that Tournemire shales present a low porosity, ranging between 6% and 10%, an average matrix density of ∼2.7 g cm^{-3} and an average density of our samples around ∼2.5 g cm^{-3}. We can note that the values of density and porosity exhibit more variability for the borehole M14 (ϕ = 90°) than others due to the vertical variability (mineralogy, grain size…) of sedimentary materials. We will consider that the parameter that will most influence the mechanical behavior is the percentage of calcite, which will induce variations in the density of the samples. We see that the densities of our samples range between 2.47 and 2.67 and that most of the values are around 2.55.

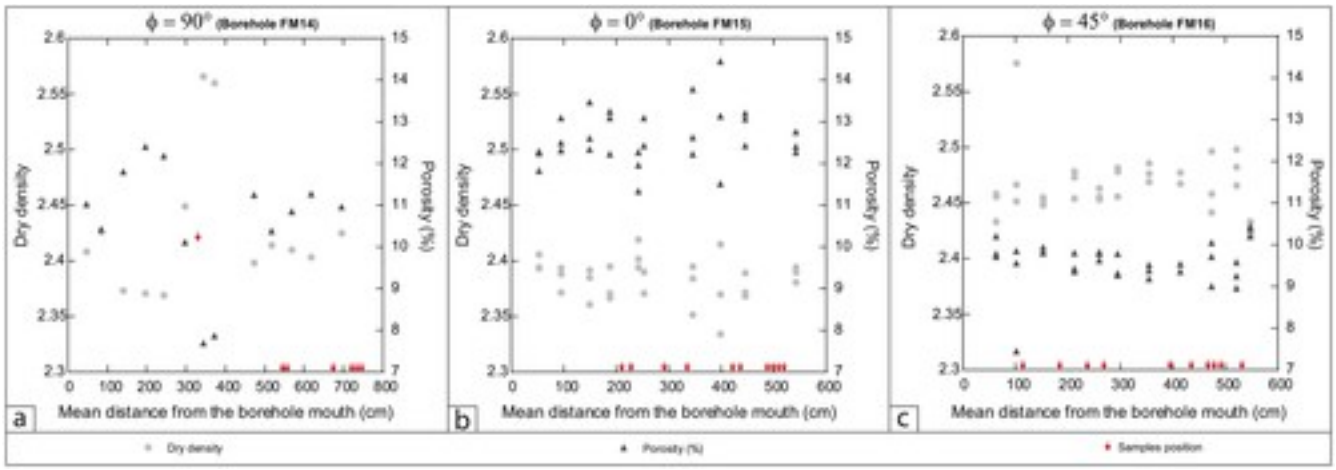

Figure 2

Open in figure viewerPowerPoint

Dry density (light grey dots) and porosity (%, dark grey triangles), measured in the field, as a function of the distance from the borehole mouth (cm), for each bedding orientation. The red squares represent the position where the samples used for mechanical tests were taken.

Because of swelling clay minerals, our samples are sensitive to humidity. In consequence, we kept them under relative humidity-controlled conditions (between 90 and 100% of ambient moisture) between each step of sample preparation. Despite these efforts, the sample saturation cannot be fully controlled during the preparation.

Cylindrical samples were dry polished, so both ends were planar and parallel, and their initial length was 82 ± 2 mm. On each sample, four pairs of strain gages (120 Ω Tokkyosokki TML FCB2-20; each pair is composed of one axial and one radial strain gage) were glued on the surface. The samples were then inserted into a viton™ sleeve for insulation from the confining fluid.

The jacket was perforated by 7 mm diameter holes, where 16 piezoelectric transducers were glued directly in contact with the sample to record the evolution of elastic wave velocities and acoustic emissions during the mechanical tests. This setup is described in a companion paper [*Bonnelye et al.*, 2017] which focuses on the evolution of elastic wave velocities.

2.2 Experimental Setup and Procedure

Experiments were performed in a triaxial oil-medium confining cell installed at the Laboratoire de Géologie of ENS Paris (Figure 3). An exhaustive description of the apparatus can be found in *Brantut et al.* [2011]. For each bedding orientation, seven confining pressures were investigated (2.5, 5, 10, 20, 40, 80, and 160 MPa). At both ends of the specimen metalic porous spacers were placed and the pore pressure system was vented to atmospheric pressure. Radial stress was maintained constant using a servo-controlled pump with an accuracy of the order of 10^{-2} MPa. First, experiments were performed at a constant strain rate of the order of $10^{-7}s^{-1}$. In order to test the rate sensitivity of the mechanical behavior, additional tests were performed at a strain rate of the order of $10^{-5}s^{-1}$ at 5 and 80 MPa confining pressures only.

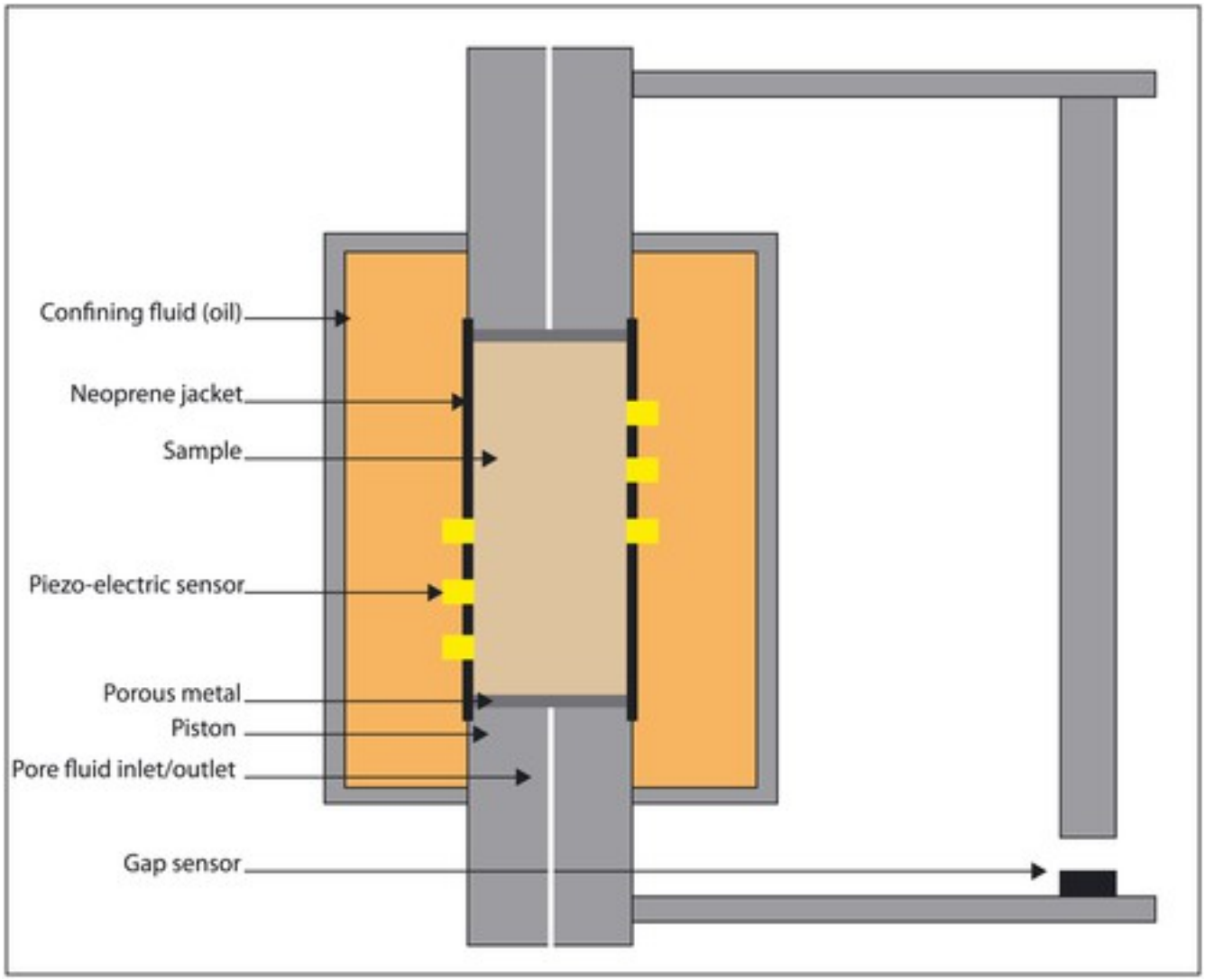

Figure 3

Open in figure viewerPowerPoint

Schematics of the triaxial apparatus at Laboratoire de Géologie of ENS Paris.

Strains were measured with four strain gage pairs (Figure 1, each composed of one axial and one radial) distributed around the sample. With our configuration, it is possible to measure two different radial strains, R1 and R2 (with redundant measurements). For $\phi = 0°$, R2 denotes the strain measured in the bedding layer, while R1 is the strain perpendicular to bedding (Figure 1). For $\phi = 90°$, those radial strains are the same. Three capacitive gap sensors were also used to measure the axial strain externally. Strain gage data, axial displacement by gap sensors, confining pressure, and axial load were recorded at 0.5–1 Hz sampling rate.

In the following material, we use both the axial strain measured with strain gages and the strain measured with the gap sensors. External strain measurement was systematically corrected from

the machine stiffness. Volumetric strain was calculated ($\varepsilon_{vol}=\varepsilon_{ax}+\varepsilon_{rad}(1) + \varepsilon_{rad}(2)$) using strain gages data for radial strain and corrected strain from gap sensors data for the axial strain.

2.3 Static Moduli Determination

We consider our material as transversely isotropic. In this case, Hooke's law can be defined as $\varepsilon = S\sigma$ (Voigt notation), where the elastic compliance matrix S is

$$S = \begin{pmatrix} \frac{1}{E_1} & \frac{-\nu_{21}}{E_2} & \frac{-\nu_{21}}{E_2} & 0 & 0 & 0 \\ \frac{-\nu_{12}}{E_1} & \frac{1}{E_2} & \frac{-\nu_{23}}{E_2} & 0 & 0 & 0 \\ \frac{-\nu_{12}}{E_1} & \frac{-\nu_{23}}{E_2} & \frac{1}{E_2} & 0 & 0 & 0 \\ 0 & 0 & 0 & \frac{1}{G_{23}} & 0 & 0 \\ 0 & 0 & 0 & 0 & \frac{1}{G_{12}} & 0 \\ 0 & 0 & 0 & 0 & 0 & \frac{1}{G_{12}} \end{pmatrix} \quad (1)$$

using the convention of Figure 4a. The E_i are the Young moduli in the direction i, ν_{ij} are the Poisson's ratios characterizing a shortening/elongation in the direction j for a compaction/dilation in the direction i, and G_{ij} are the shear moduli in the plane (i,j).

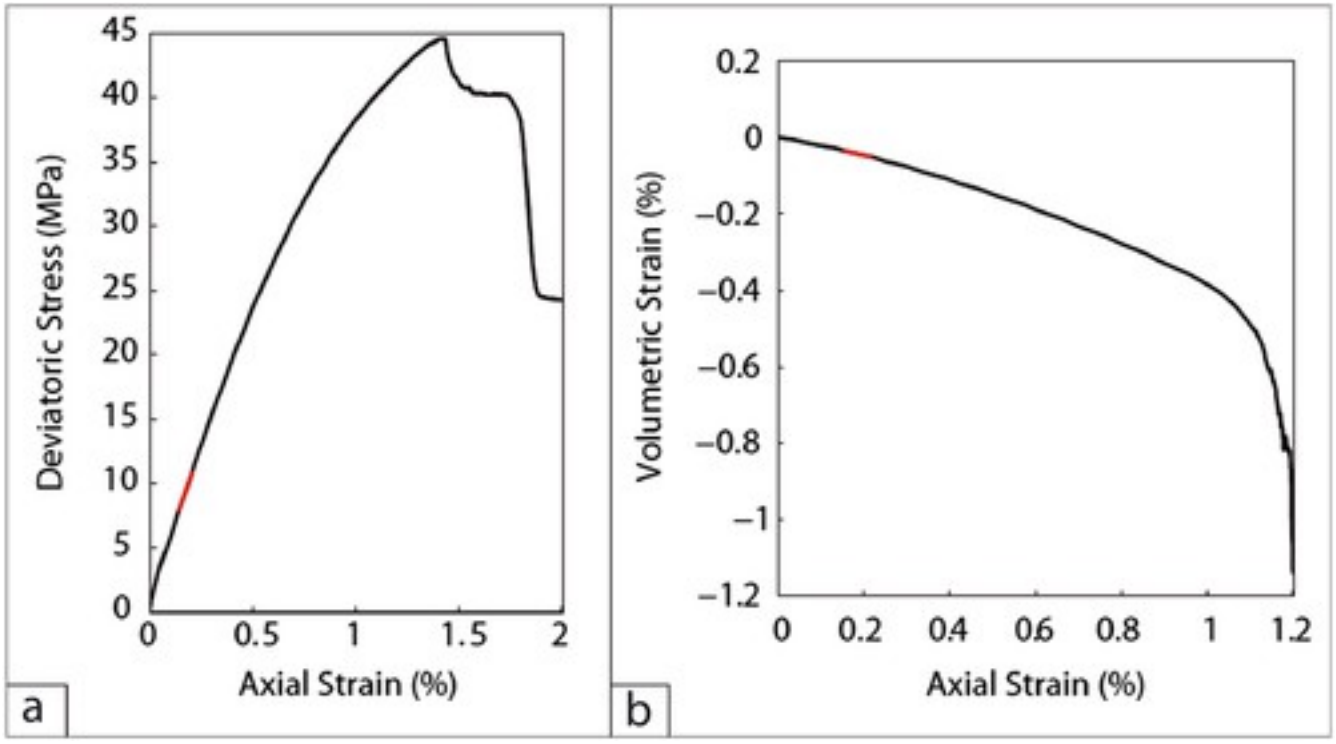

Figure 4

Open in figure viewerPowerPoint

(a) Deviatoric stress (MPa) versus axial strain (%) plot to calculate Youngs modulus and (b) radial strain (%) versus axial strain (%) to calculate Poisson's ratio. Linear regressions (in red) to obtain the elastic moduli at each confining pressure correspond to the range 20–25% of peak stress.

The elastic parameters shown here are tangent moduli. For Young moduli, we made a linear regression on axial strain/deviatoric stress curves between 20 and 25% of peak stress (Figure 4a). The Poisson's ratios are then determined by a linear regression on the same interval on the axial strain versus radial strain plot (Figure 4b).

During each experiment, three tangent moduli were measured: the apparent Young's modulus along the compression axis and two Poisson's ratios, respectively, v_1 calculated with the strain gage R1 and v_2 calculated with the strain gage R2. The apparent Young modulus calculated for $\phi = 90°$ orientation is E_1 and the apparent Young modulus calculated for $\phi = 0°$ is E_2. The three Poisson's ratios that we are able to determine are v_{12} with the $\phi = 90°$ orientation, v_{23}, and v_{21} with the $\phi = 0°$ orientation. G_{12} can be determined with the $\phi = 45°$ orientation either with the relashionship $G_{12}=E_{45°}/2(1 + v_{45°})$ or with $G_{12}^{-1} = 1/E_1 + 1/E_2 + 2v_{12}/E_1)$ from *Kachanov* [1992].

All those moduli, presented in Table 2, are “apparent,” because as we will see in the following material, Tournemire shale does not exhibit clear elastic phase (i.e., a linear phase of reversible

deformation). In consequence, these apparent moduli are lower bounds for $E_i$and G_{ij} and upper bounds for ν_{ij} that probably include a nonnegligible amount of inelastic deformation.

Table 2. Synthesis of the Sample's Parameters and Strain Rate Used for Each Experiment

	Sample Length (mm)	Diameter (mm)	Volume (cm3)	Sample Weight (g)	Sample Density	Str
ϕ=90°	84.94	41.37	114.18	292.76	2.56	2
	81.68	41.34	109.63	270.82	2.47	3
	80.69	41.34	108.31		0	2
	82.58	41.4	111.16	280.54	2.52	5
	82.97	41.39	111.64	281.22	2.52	5
	82.24	38.19	94.20	253.66	2.69	4
	81.75	41.4	110.05		0	3
	80.34	41.36	107.94	286.86	2.66	4
ϕ=0°	83.76	41.32	112.32		0	2

	Sample Length (mm)	Diameter (mm)	Volume (cm3)	Sample Weight (g)	Sample Density	Str
	83.88	41.21	111.88	284.94	2.55	2
	80.28	41.37	107.91	273.96	2.54	2
	83.89	41.31	112.44	287.52	2.56	2
	83.81	41.32	112.38		0	3
	80.2	41.35	107.70		0	3
	83.35	41.22	111.23	283.16	2.55	3
	83	41.34	111.41		0	4
ϕ= 45 ∘	82.24	41.3	110.17	276.72	2.51	5
	82.5	41.2	109.99		0	2
	80.28	41.25	107.29	273.34	2.55	2

	Sample Length (mm)	Diameter (mm)	Volume (cm3)	Sample Weight (g)	Sample Density	Str
	83.64	41.2	111.51	282.2	2.53	3
	81.75	41.093	108.42	277.96	2.56	4
	80.84	41.35	108.56	272.52	2.51	4
	82.47	41.5	111.55		0	4
	80.28	41.37	107.91	272.58	2.53	5

3 Results

3.1 Mechanical Behavior During Deviatoric Loading

3.1.1 Axial Strain and Strength

Stress-strain curves for the three bedding orientations are displayed in Figure 5, and peak stress and dilatancy stress are displayed in Table 3 for confining pressures of 2.5, 5, 10, 20, 40, 80, and 160 MPa. The mechanical behavior of Tournemire shale is strongly impacted by the direction of loading with respect to the bedding.

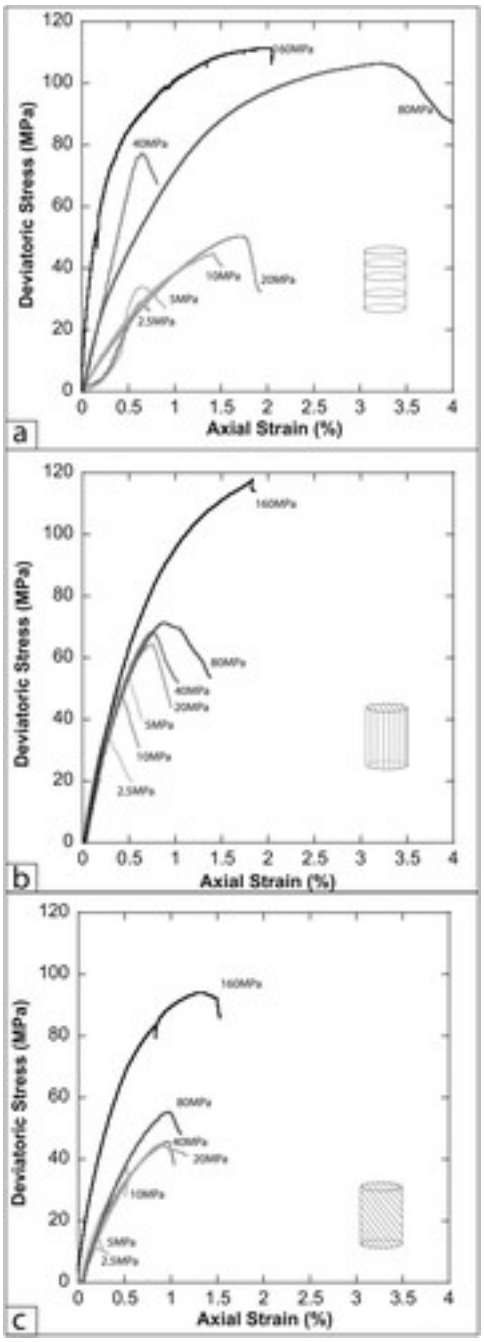

Figure 5

Open in figure viewerPowerPoint

Deviatoric stress ($\sigma_1-\sigma_3$, MPa) as a function of axial strain (%), for experiments performed along three bedding orientations: (a) ϕ = 90°, (b) ϕ = 0°, and (c)ϕ = 45°. Gray scale corresponds to the confining pressures investigated: 2.5, 5, 10, 20, 40, 80, and 160 MPa, from light grey for low confining pressures to black for high confining pressures.

Table 3. Peak Stresses (MPa) and Value of Deviatoric Pressure at Dilation (*D*') as a Function of Confining Pressure and Bedding Orientation

Bedding Orientation (ϕ)	P_c (MPa)	Q_{peak} (MPa)	D' (MPa)
90	2.5	29.1	12
	5	34.1	32.8
	10	44.58	35.4
	20	50.39	50
	40	77.5	65.3
	80	106.48	85.7
0	2.5	35.31	15.3
	5	53.32	19
	10	48.04	22
	20	64.35	40.8
	40	68.27	68
	80	71	42.4

Bedding Orientation (ϕ)	P_c (MPa)	Q_{peak} (MPa)	D' (MPa)
45	2.5	11.26	–
	5	14.85	13.6
	10	37.46	25
	20	45.7	22.2
	40	56.78	40
	80	55.23	32.6

For samples that deformed perpendicular to bedding (ϕ = 90°, Figure 5a) we observe increasing value of peak stress from around 25 MPa at P_c=2.5 MPa to around 110 MPa at P_c=160 MPa. For the lowest confining pressures (2.5 and 5 MPa), the initial part of the stress-strain curve is highly nonlinear, with important axial deformation observed for moderate increase of deviatoric stress. This is probably due to crack closure and to recompaction of the bedding planes that may have been disturbed by drilling. This may explain the dispersion of the initial “elastic” loading documented in Table 4.

Table 4. Tangent Elastic Moduli (Calculated Between 20% and 25% of Peak Stress) as a Function of Confining Pressure and Bedding Orientation

P_c (GPa)	E_1	E_2 (GPa)	ν_{12}	ν_{21}	ν_{32}	G_{21} (GPa)	G_{23}
2.5	4	10.4	0.19	0.34	0.14	1.5	4.6

P_c (GPa)	E_1	E_2 (GPa)	ν_{12}	ν_{21}	ν_{32}	G_{21} (GPa)	G_{23}
5	4	12.7	–	0.6	0.2	3.3	5.3
10	4.6	16.4	0.25	0.43	0.1	2.8	7.4
20	4.6	13.4	0.16	0.75	0.28	2.9	5.3
40	15.4	–	0.24	–	–	2.6	–
80	9.7	12.5	0.17	0.42	0.1	3.1	5.7

Samples cored parallel to bedding (ϕ = 0°, Figure 5b) exhibit increasing peak stress with increasing confining pressure. The peak stress increases from 30 MPa for P_c=2.5 MPa to 118 MPa for P_c=160 MPa. All the samples cored in this orientation exhibit smaller axial deformation to reach peak compared to those cored at ϕ = 90°. Contrarily to the previous orientation, there is little dispersion in the value of the Young's modulus (Table 4).

For samples deformed at 45° (Figure 5c) peak stress increases with increasing confining pressure, from 11 MPa for P_c=2.5 MPa to 98 MPa for P_c=160 MPa with increasing Young's moduli with confining pressure and little axial deformation.

In summary, the failure mode remains brittle at all confining pressures for the three orientations, the orientation ϕ = 45° being the weakest. Increasing plastic deformation seems to occur before peak stress at higher values of confining pressure (from P_c=40 MPa), in particular for ϕ = 90°. Failure is always accompanied by slow stress drop (of the order of second and more) and by no detectable acoustic emission, at least in the frequency range investigated (0.1–1 MHz). Stress drops also decrease with increasing pressure and are minimal for the orientation at 45°. Axial deformation is largest in the case of the 90° orientation, meaning that voids between the bedding planes accommodate a large amount of the deformation, whereas in the case of the 0°

orientation, all the deformation is accommodated by the bedding layers, as it is always the most rigid layer that supports the most important load in this configuration [*Tien and Kuo*, 2001].

3.1.2 Radial Strain Anisotropy

As we measure the deformation at four locations around the sample, it is possible to study the strain anisotropy. Radial strains are presented as a function of axial strain for orientations ϕ = 90°, ϕ = 0°, and ϕ = 45° in Figures 6a–6c, respectively. For ϕ = 90°, the radial deformation is similar at R1 and R2 locations, and much smaller than axial deformation, with apparent Poisson ratio's ν_{12} ranging from 0.16 to 0.25.

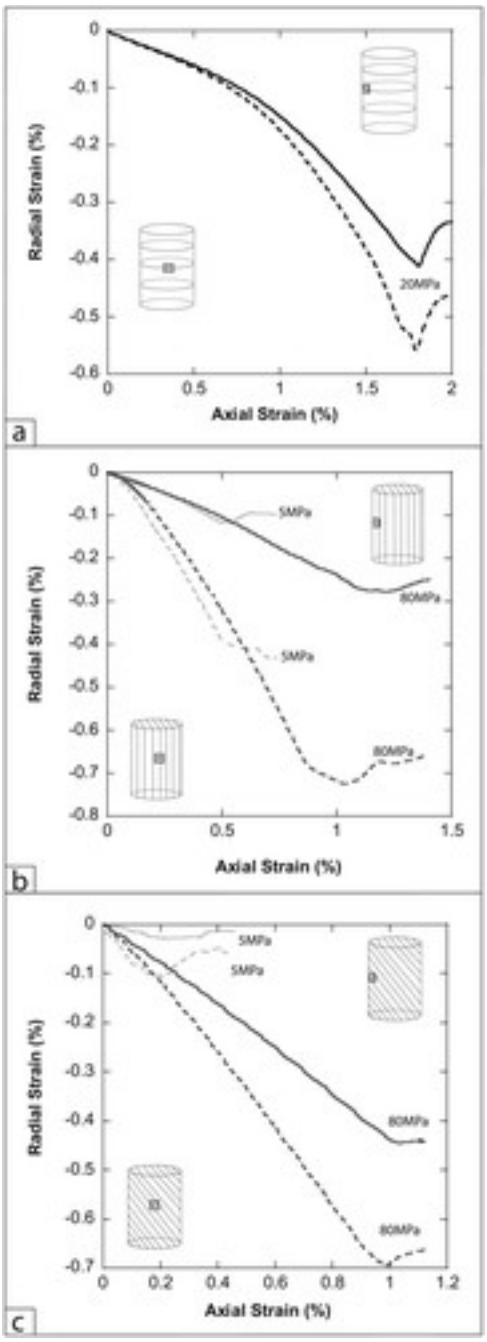

Figure 6

Open in figure viewerPowerPoint

Radial strain (%) as a function of axial strain (at the locations R1 (dashed lines) and R2 (solid lines)) for three bedding orientations: (a) for ϕ = 90° and confining pressure 20 MPa, (b) for ϕ= 0° and confining pressures 5 and 80 MPa, and (c) for ϕ = 45° and confining pressures 5 and 80 MPa.

On the contrary, for ϕ = 0°, the two radial deformations are different. Radial strains measured across bedding (R1) are close to axial strain so that along this direction, the apparent Poisson's ratio v_{21} is generally larger than 0.3 and sometimes even to 0.5. This is certainly due to nonelastic

deformation and in particular to the opening of the bedding with increasing applied stress. This effect seems to decrease slightly with increasing confining pressures. On the contrary, radial strains measured within the bedding (R2) remain low compared to axial strain, with almost constant apparent Poisson's ratio v_{23} below 0.2.

The orientation ϕ = 45° exhibits an intermediate behavior, with decreased apparent radial anisotropy relative to ϕ = 0°. In this case, the Poisson's ratios that we can calculate have no meaning for transversely isotropic medium because no strain gage is oriented in the bedding plane or parallel to the bedding plane. The data are just shown in order to have an idea of the evolution of deformation.

3.1.3 Volumetric Deformation

The evolution of volumetric deformation is also strongly impacted by bedding orientation. However, it is important to keep in mind that the volumetric deformations are calculated with an average of R1 and R2 deformations (as defined in section 2.3) and so they only represent an average volumetric strain.

For the 90° orientation (Figure 7a) the main deformation undergone by the sample is compaction (between 0.2 and 0.6%), followed by shear-induced dilatancy. The onset of dilatancy *C*' is difficult to measure in these experiments because the stress-strain curves are highly nonlinear. For this reason, we use the transition to dilatancy *D*' (i.e., the peak of compaction) as a proxy for *C*' [*Heap et al.*, 2009]. The maximum of compaction is reached for the experiment at 20 MPa confining pressure. For the confining pressure 80 MPa, dilatancy appears at around 2% percent of axial strain, clearly indicating the appearance of plastic mechanisms (crack propagation). As we observe mostly compaction, it is in good agreement with data for axial strain shown in the previous section, meaning that the deformation is mostly accommodated by the interlayer voids.

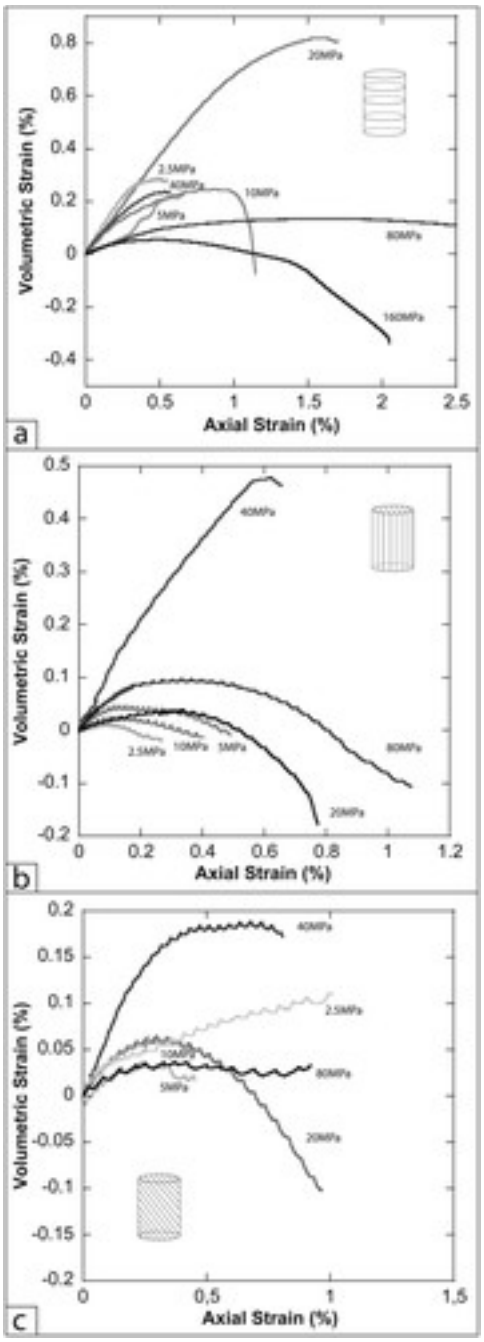

Figure 7

Open in figure viewerPowerPoint

Volumetric strain (%) as a function of axial strain (%), for experiments performed along three bedding orientations: (a) ϕ = 90°, (b) ϕ = 0°, and (c) ϕ = 45°. Gray scale corresponds to the confining pressures investigated: 2.5, 5, 10, 20, 40, and 80 MPa (and 160 MPa for ϕ = 90° and ϕ = 0°), from light grey for low confining pressures to black for high confining pressures.

The samples with orientation 0° show no more compaction than 0.1% (except for the test at 40 MPa) and the largest amount of dilatancy. This trend increases with confining pressure, and again, *D*' is reached at increasing axial strain with increasing confining pressure. Finally, for the

45° orientation little volumetric deformation is observed. Nevertheless, *D*' is systematically followed by shear-enhanced dilatancy.

3.1.4 Influence of Strain Rate

Strain rate plays an important role both in the values of tangent elastic moduli and in the peak stress [*Peng and Podnieks*, 1972].

The experiments shown previously were conducted at a strain rate of the order of $10^{-7}s^{-1}$. To test the impact of strain rate on the mechanical behavior, additional experiments were performed at a strain rate of the order of $10^{-5}s^{-1}$. For each orientation, two confining pressures (5 MPa and 80 MPa) are compared in Figures 8 (stress-strain curves) and 9(volumetric strain-axial strain curves). Orientations 90° and 0° (Figures 8a–8d and 9a and 9b) both display a significative strain rate dependence.

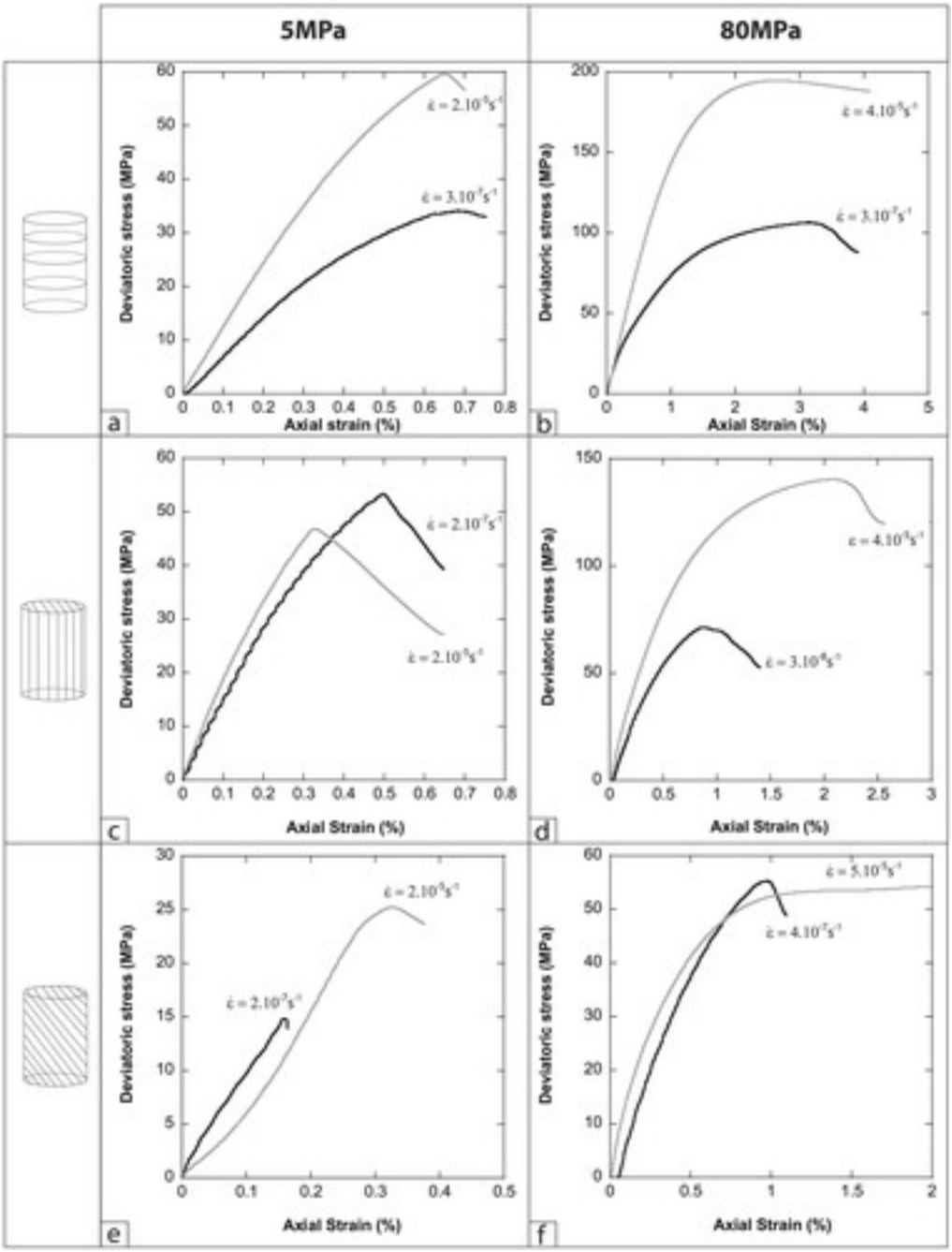

Figure 8

Open in figure viewerPowerPoint

Deviatoric stress ($\sigma_1-\sigma_3$, MPa) as a function of axial strain (%) for confining pressures of (a, c, and e) 5 MPa and (b, d, and f) 80 MPa and for three bedding orientations ϕ = 90° (Figures 8a and 8b), ϕ = 0° (Figures 8c and 8d), and ϕ = 45° (Figures 8e and 8f), high strain rate (grey curve) and low strain rate (black curve).

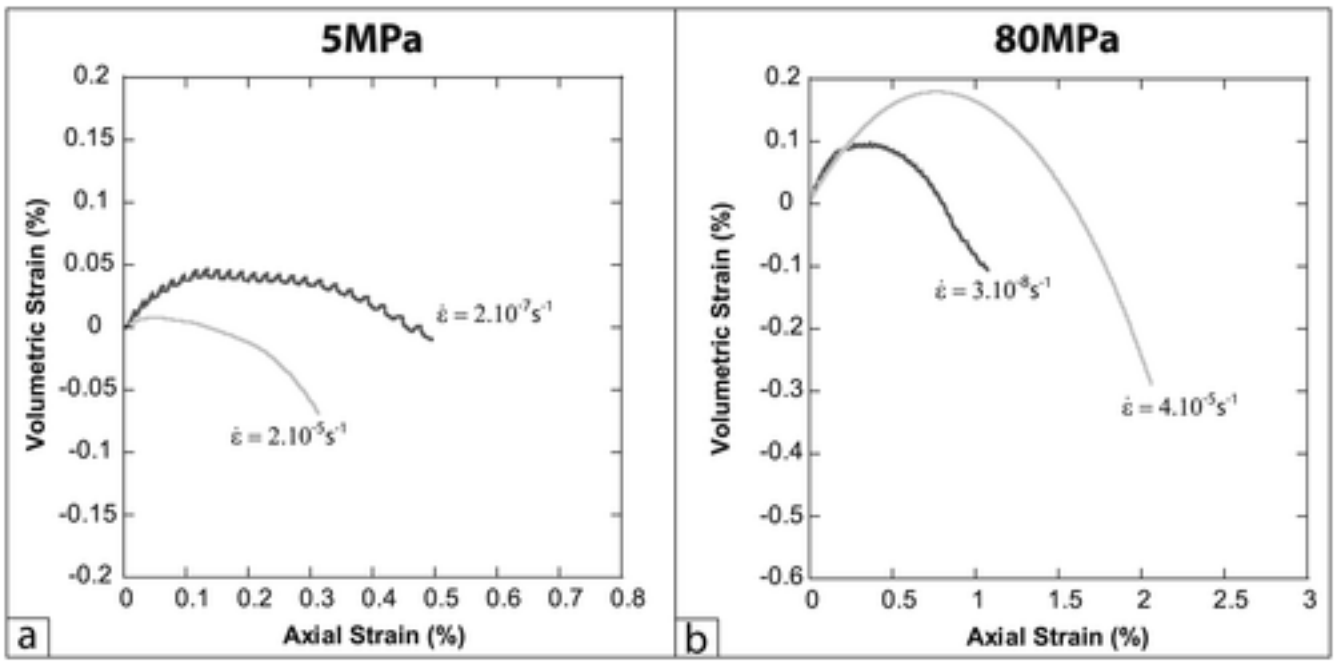

Figure 9

Open in figure viewerPowerPoint

Volumetric strain (%) as a function of axial strain (%) for confining pressures of (a) 5 MPa and (b) 80 MPa and for bedding orientation ϕ = 0°, high strain rate (grey curve), and low strain rate (black curve).

First, the apparent Young's modulus increases with strain rate, meaning that the faster the strain rate, the stiffer the rock. We also observe that longer nonlinear phases occur which indicates that more plastic strain, in this case, mostly cracks, takes place in the material before failure.

Second, peak stress is also strain rate dependent. For ϕ = 90°, the impact is similar at low and high confining pressures and the peak stress increases almost twice at higher strain rate. For ϕ = 0°, strain rate dependence is larger at high confining pressure.

Third, more dilatancy is observed at high strain rate so that the deformation is probably associated with larger amount of crack propagation.

The orientation 45° seems to exhibit a smaller strain rate dependence in terms of elasticity and strength, in particular at higher confining pressure. Since for this orientation the maximum shear stress is in the bedding, we conclude that frictional sliding in between bedding planes exhibits close to no strain rate dependence. On the contrary, because orientations deformed perpendicularly and parallel to bedding exhibit large strain rate dependence, and because the fracture for these orientations cuts through the bedding planes (see section 3.2), we suggest that the cohesive strength, in other words, the strength needed to fracture across bedding and the mineral bonds, is strain rate dependent.

3.2 Microstructures

The samples were soaked in epoxy and sliced in order to see the evolution of strain localization with increasing confining pressure (Figures 10 and 11).

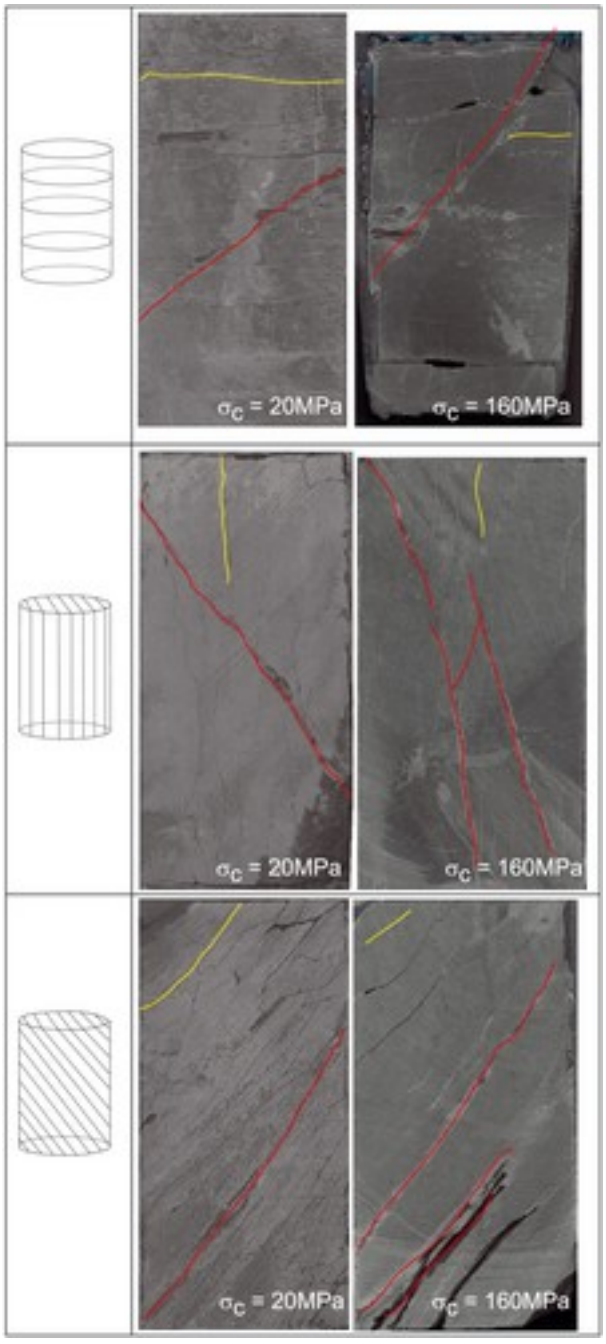

Figure 10
Open in figure viewerPowerPoint
Postmortem images of fractured samples for confining pressures of (left column) 20 MPa and (right column) 160 MPa. Three bedding orientations are shown: (top row) ϕ = 90°, (middle

row) $\phi = 0°$, and (bottom row) $\phi = 45°$, all deformed at low strain rate. The bedding orientation is highlighted in yellow, the fractures in red.

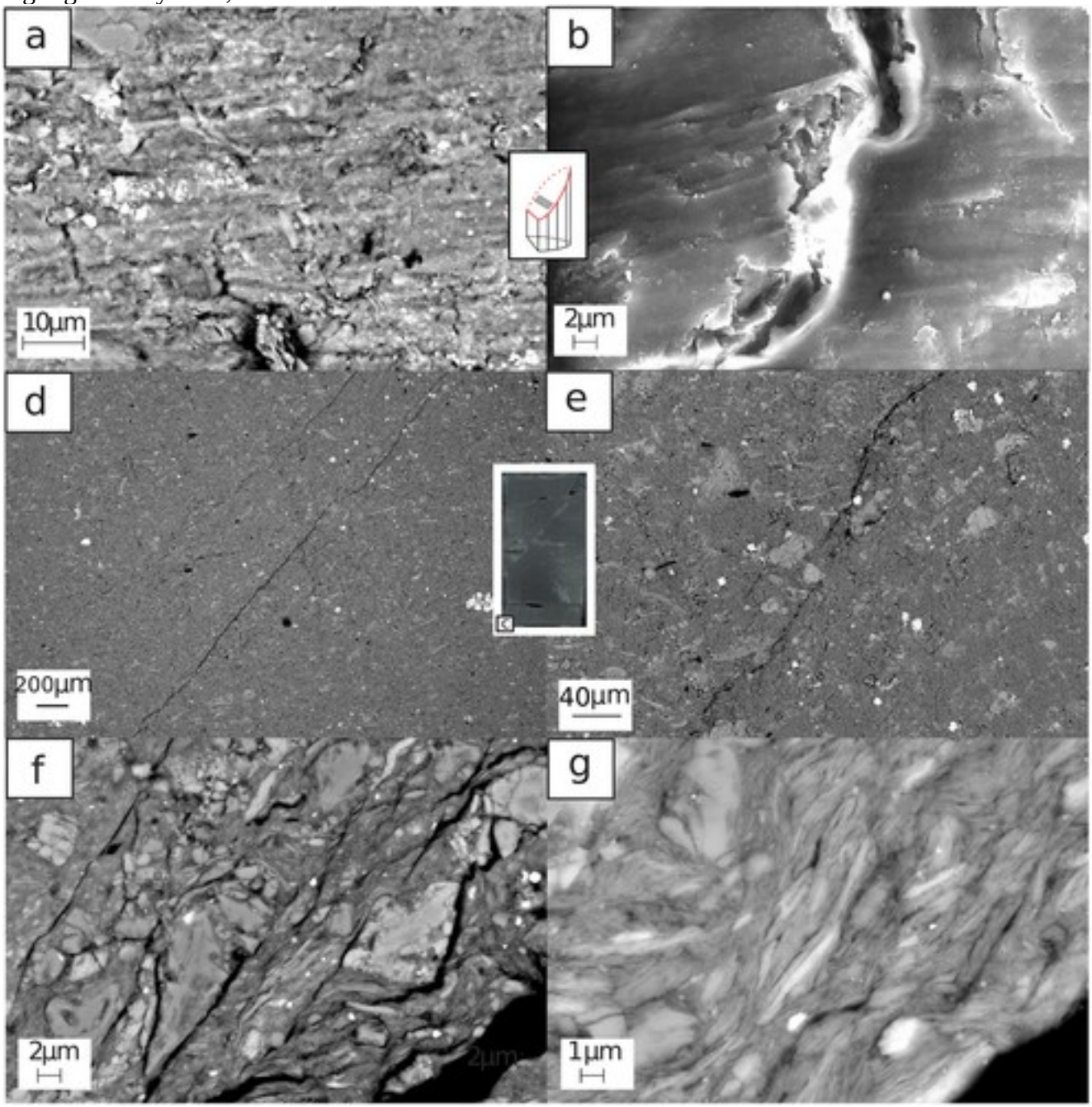

Figure 11

Open in figure viewerPowerPoint

(a and b) Scanning electron micrograph of the fracture plane of sample deformed parallel to bedding ($\phi = 0°$) and 80 MPa confining pressure at a strain rate of $3 \times 10^{-5} s^{-1}$. (c–g) Fracture on a sample deformed perpendicular to bedding ($\phi = 90°$) at 160 MPa confining pressure.

For the orientation $\phi = 90°$, the fracture is always localized in a single fracture. But for the experiment performed at a confining pressure of 160 MPa, we can see evidences of both fragile and ductile regimes, with the coexistence of a throughgoing fracture and barreling.

For the orientation $\phi = 0°$, the fracture is well localized along a single plane through the bedding. At high confining pressures, a fracture network appears as an evidence of increased plasticity, in this case, more crack propagation.

For the orientation $\phi = 45°$, the fracture is always parallel to the bedding plane. The bedding is in this case planes of weakness, aligned with the maximum shear stress.

Scanning electron microscope (SEM) images were taken on deformed samples (Figure 11), in order to gain further insights on the microstructure in the fracture plane.

The fracture surfaces of a sample deformed parallel to bedding ($\phi = 0°$), at 80 MPa confinement and at high strain rate (Figures 11a and 11b) show slip marks, which illustrate the slip on the fracture plan. The slip causes grain reorientation on the fault plan but seems to only affect a very thin layer. Indeed, beneath this layer, a few micron thick only, we observe minerals with the initial bedding orientation. Nevertheless, it is interesting to point that these slip marks were produced at relatively low strain rates, and aseismically, as no AE were detected at failure and are thus not markers of seismic deformation.

We also looked at the microstructures of the sample deformed at low strain rate with a confining pressure of 160 MPa. We note that what was considered to be a single fracture at the sample scale looks more like a coalescence of cracks at the microscale (Figures 11d and 11e). Finally, we observe at lower scale that there is platelet reorientation parallel to the fault surface (Figures 11f and 11g).

Additional microstructures can be found in *Bonnelye et al.* [2017].

4 Discussion

4.1 Plastic Yield Envelopes

The failure criterion of a material is fundamental to understand its mechanical behavior. In the case of Tournemire shale, we have shown that samples undergo brittle failure, for all orientations, over the range of confining pressure investigated here, which is 2.5–160 MPa.

We observe, as shown by previous studies, that Tournemire shale exhibits a strong mechanical strength anisotropy, the orientation $\phi = 45°$ being the weakest, $\phi = 0°$ the intermediate, and $\phi = 90°$ the strongest (Figure 13, A). Here we compare to kinds of linear criterion, one based on the wing crack theory, described below, and a Mohr-Coulomb type.

The wing crack theory, given by *Kachanov* [1980] and then *Ashby and Sammis* [1990], can be written as

$$\sigma_1 = \frac{(1+\mu^2)^{1/2}+\mu}{(1+\mu^2)^{1/2}-\mu}\sigma_3 - \frac{\sqrt{3}}{(1+\mu^2)^{1/2}-\mu}\frac{K_{Ic}}{\sqrt{\pi l}} \quad (2)$$

where μ is the internal friction coefficient, K_{Ic} is the fracture toughness, and l is the length of the initial flaw. As this criterion denotes the moment when cracks open in the medium, it should be written using the stress at which the volumetric strain deviates from linearity at the beginning of dilatancy, C^*. In our case, due to the nature of our material, the transition from linearity to nonlinearity is hard to determine so we decided to use the dilation D' point reported in the radial stress (σ_1)-axial stress (σ_3) plane; we can note that our data can be fitted with a linear curve in Figure 12a. In order to determine the internal friction coefficient and the length of the initial flaw from equation 2, we used values of *Chandler* [2015] who found values around ~0.6 on Mancos Shale. The values for each orientation are presented in Table 5. We found values of internal coefficient between 0.1 and 0.3 and of initial flaw of the order of 10^{-5} m.

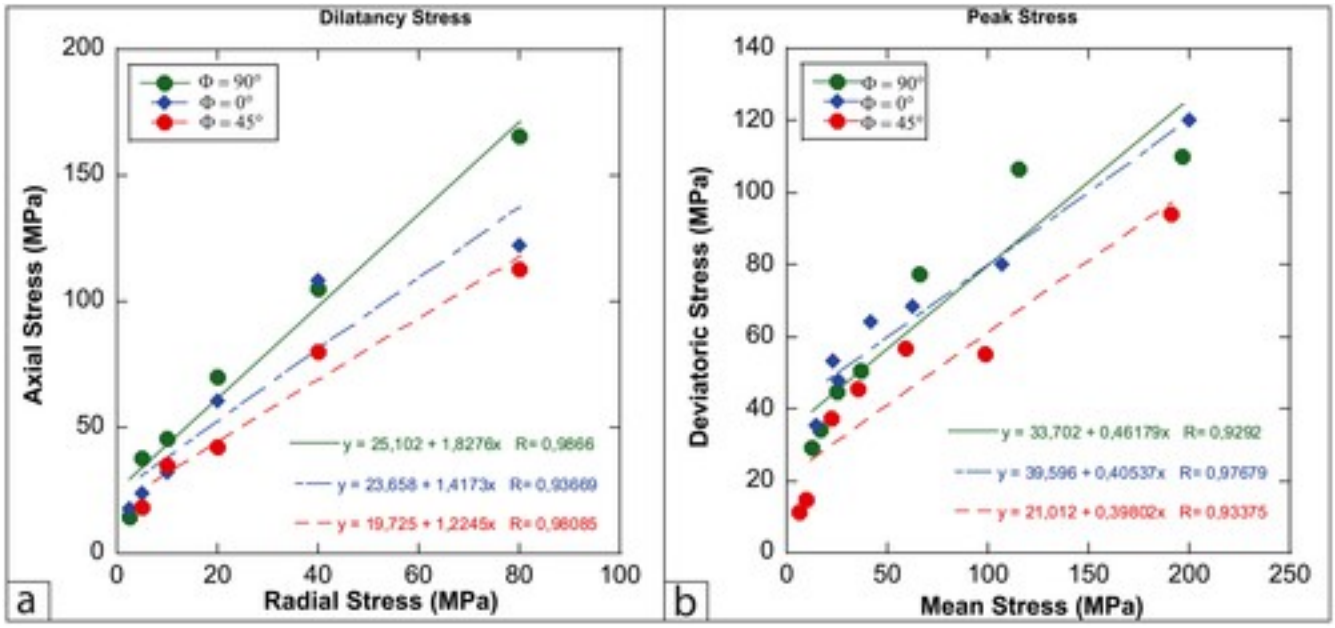

Figure 12

Open in figure viewerPowerPoint

Fit of envelopes for (a) the transition to dilatancy in the radial stress-axial stress plane and (b) the peak stress in the mean stress-deviatoric stress plane.

Table 5. Friction Values and Fracture Toughness [From *Ashby and Sammis*, 1990] and Apparent Friction Coefficient

ϕ	Internal Friction Coefficient	Apparent Friction Coefficient	K_{Ic} (MPa m$^{1/2}$)	l (m)
ϕ = 90°	0.31	0.27	0.72	0.0006
ϕ = 0°	0.18	0.23	0.72	0.0007
ϕ = 45°	0.10	0.23	0.21	0.0003

We also calculated the Mohr-Coulomb-type friction coefficient using the slope ($a/\sqrt{3}$) of the envelope (peak stress in the mean stress ($\frac{\sigma_1+2\sigma_3}{3}$)- deviatoric stress plane($\sigma_1-\sigma_3$)). These results are all presented in Table 5. We obtained low friction coefficient values (between 0.23 and 0.27) that are in good agreement with friction coefficients determined experimentally by *Saffer and Marone* [2003] in illite and smectite.

Moreover, we see that with the two different methods we obtain similar values of friction coefficient. They do not have exactly the same meaning: the internal friction coefficient is more local, expressing a mineral to mineral sliding, whereas the Mohr-Coulomb friction coefficient takes into account the whole sample. As the values found are close from each other, we can conclude that the friction in shales is controlled by the amount of clay in the material.

However, the reduction of anisotropy with increasing confining pressure is not straightforward. As shown in Figure 13, which compares ratios of peak strength measured at failure between the orientations ϕ = 90° and ϕ = 45° with other studies of anisotropic rocks, there is a decrease of anisotropy at low confining pressures (from 0 to 20 MPa) followed by an increase up to a ratio of 2 between 20 and 80 MPa and then another decrease.

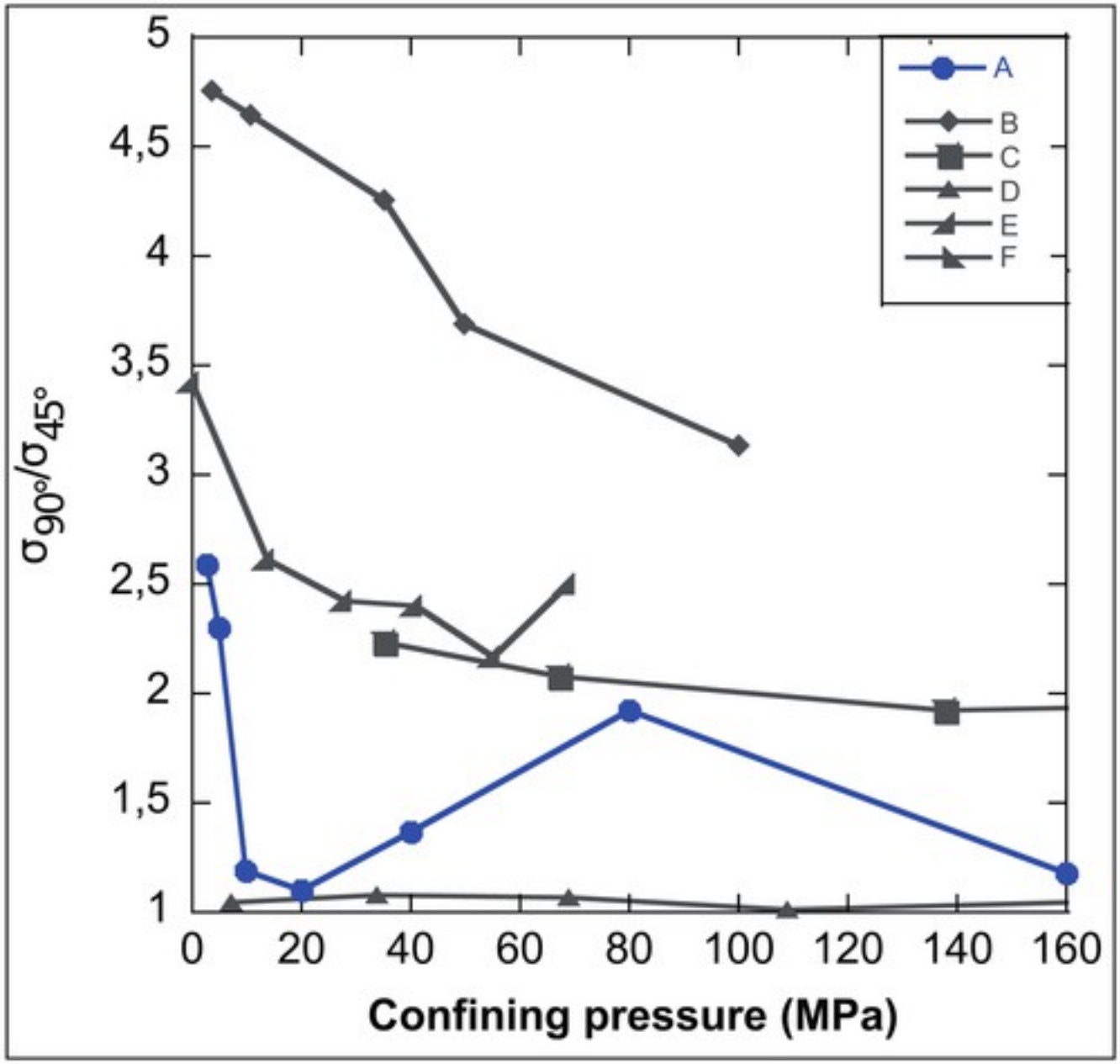

Figure 13

Open in figure viewerPowerPoint

Ratios of peak deviatoric stress for the orientation 90° to peak deviatoric stress for the orientation 45° with A: our data at slow strain rate, B: Martinsburg slate from *Donath and Parker* [1964], C: Austin slate from *McLamore and Gray* [1967], D: Green River shale from *McLamore and Gray* [1967], E: Blue Penrhyn slate from *Attewell and Sandford* [1974], and F: limestone from *Horino and Ellickson* [1970].

4.2 Influence of Strain Rate

Figure 14 displays the plastic yield envelopes, including our data and data from previous studies, in the deviatoric stress ($\sigma_1-\sigma_3$) mean stress ($(\sigma_1+2\sigma_3)/3$) space, for each bedding orientation. Our

results are compared with previous mechanical studies performed on Tournemire shale [*Barbreau et al.*, 1994; *Niandou et al.*, 1997; *Abdi et al.*, 2015]. We see that at low confining pressures (2.5, 5, and 10 MPa), our experimental results are in good agreement with the previous ones, for all bedding orientations. However, for higher confining pressures, our values of peak stress are systematically lower than the values obtained by former studies. At first glance, this mechanical behavior could either be a result of (i) a weakening due to a saturation better than in the previous studies, as our sample had been drilled directly at the right diameter (i.e., no overcoring) and then conserved in pristine conditions, or (ii) a strain rate effect, as most previous studies were performed at strain rate orders of magnitudes faster (typically $10^{-5}s^{-1}$) than the ones performed here ($10^{-7}s^{-1}$). In the first case, the weakening would have been observed for all confining pressures. In the second case, either the cohesion or the friction, or both, could exhibit important rate dependence.

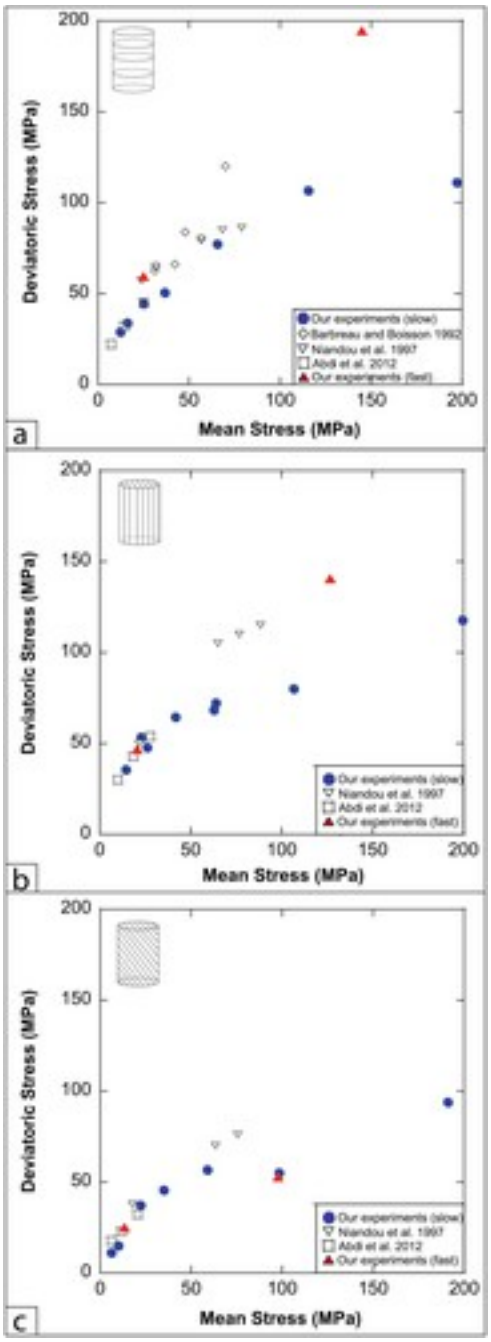

Figure 14

Open in figure viewerPowerPoint

Plastic yield envelopes for the three bedding orientations: (a) $\phi = 90°$, (b) $\phi = 0°$, and (c) $\phi = 45°$. Peak stresses are plotted in the deviatoric stress ($\sigma_1 - \sigma_3$, MPa) mean stress ($(\sigma_1 + 2\sigma_3)/3$, MPa) space and compared to data from previous studies on Tournemire shale by *Barbreau et al.* [1994], *Niandou et al.* [1997], and *Abdi et al.* [2015].

To test one of these hypotheses, higher strain rate ($10^{-5}s^{-1}$) experiments were performed and these were found to be rather in the same trend than previously published experiments. The strain rate effect can be explained by time-dependent plasticity mechanisms (cracks propagation and

mineral reorientation), which are more important during slow deformation, or by undrained conditions during rapid deformation.

We performed the calculations proposed by *Duda and Renner* [2012] in order to determine the status of our samples (drained or undrained), by defining a critical strain rate above which the experiments are under undrained conditions:

$$\dot{\epsilon_{cr}} = \frac{0.1 D_{hyd} \epsilon_f}{l^2} \quad (3)$$

where $\dot{\epsilon_{cr}}$ denotes the critical strain rate, D_{hyd} is the hydraulic diffusivity, ε_f is the strain at failure, and l is the sample length.

Over the permeability range of our samples (between 10^{-20} and 10^{-21}m^2), strain rates used during our experiments cause undrained deformation (Figure 15). The observations on postmortem samples show for high confining pressures that the sample exhibits evidences of both fragile and ductile regimes (Figure 11c). In addition, when looking at SEM images, we noted that the main fracture is not continuous but looks like a relay fault at the sample's scale and that there is a band in which the minerals are reoriented (Figures 11f and 11g). Moreover, the elastic wave velocities presented in *Bonnelye et al.* [2017] confirm the presence of plasticity mechanisms, such as mineral reorientation and cracks propagation, for slow strain rate experiments, and we can infer, as we observe more dilatancy during fast experiments, that cracks are formed in order to accommodate the deformation. Finally, strain rate dependence is observed only for samples deformed perpendicularly and parallel to bedding, while samples deformed at 45° exhibit little to no strain rate dependence. This implies that the strain rate dependence is mainly due to fracture toughness K_{Ic}, and one can thus conclude that K_{Ic} in shales is not only simply anisotropic [*Chandler*, 2015] but also strongly strain rate dependent.

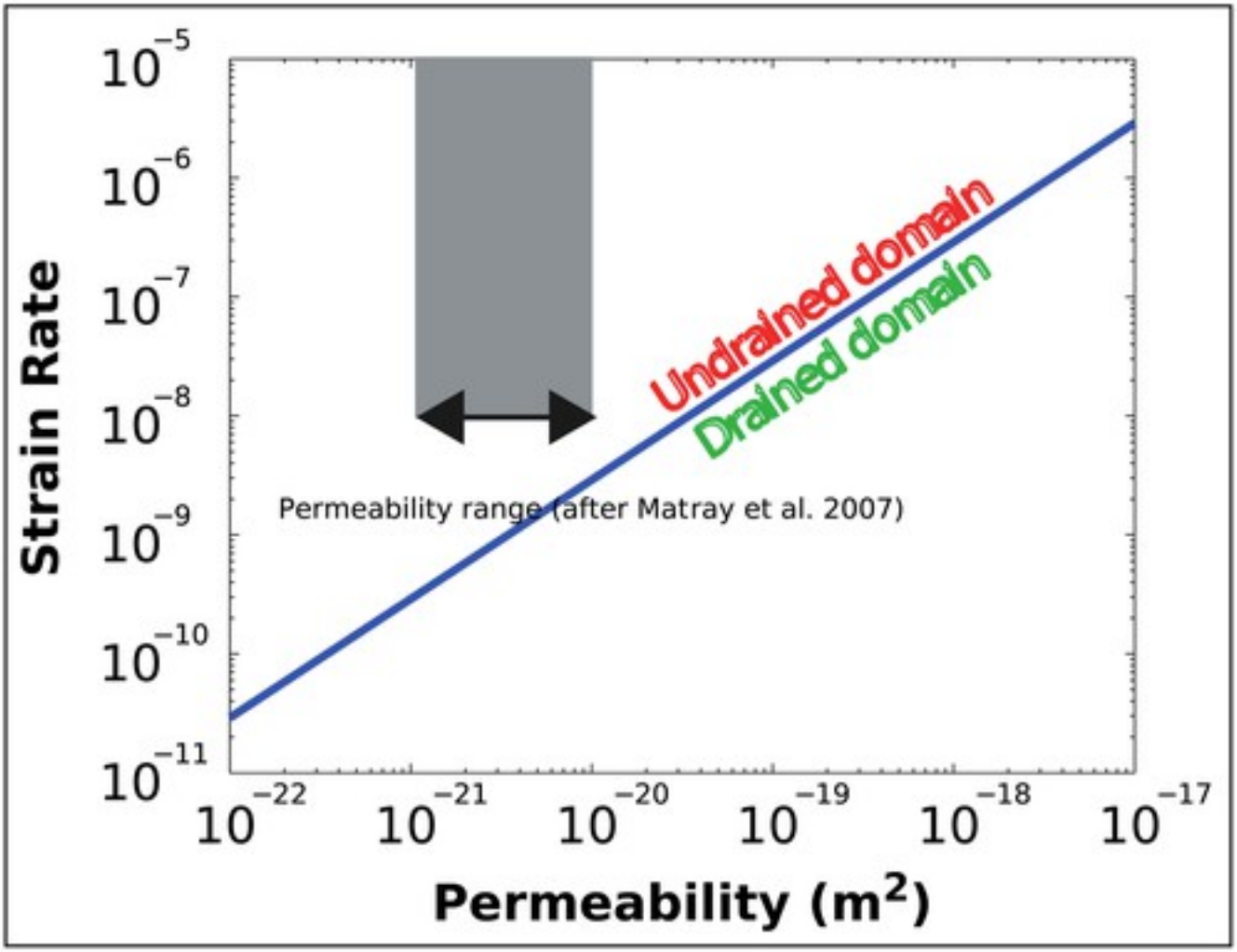

Figure 15

Open in figure viewerPowerPoint

Critical strain rate line as a function of permeability (m^2) from *Duda and Renner* [2012] equation. The grey shaded area represents the domain in which the experiments were performed here.

Finally, all our experiments were done without control of saturation and pore fluid pressure, which of course plays a crucial role on fault mechanics [*Sibson*, 1973; *Rice*, 1992; *Wibberley and Shimamoto*, 2003, 2005]. But shales, because of their swelling properties and low permeability, are extremely difficult to deform in the laboratory under controlled saturated conditions. Yet *Vals et al.* [2004] studied the influence of saturation on mechanical properties of shales and showed that shales tend to be mechanically weaker but that full saturation seems to only have a limited impact on the anisotropy of elastic properties. More experiments need to be performed to delve deeper into our understanding of the mechanical behavior of shales.

5 Conclusions

In terms of mechanical strength, we have shown that the bedding orientation has a strong impact on peak stress, with the orientation $\phi = 45$ the weakest and $\phi = 90°$ the strongest. We have also shown that this is enhanced both by the strain rate and by confining pressure. The strain rate seems to also affect the thickness of the fault zone: the faster the deformation occurs, the thinner the fault zone. The way fracture develops in the sample depends on the bedding orientation. For the orientation $\phi = 90°$, we observed that fracture occurs through the bedding plane for all confining pressure. The orientation $\phi = 0°$ breaks along the bedding planes at low confining pressures and through the bedding planes when the confining pressure increases. Finally, the orientation $\phi = 45°$ seems to always break along the bedding plane as it is aligned with the maximum shear stress.

Moreover, we showed that it is possible to explain our data set with simple micromodel such as wing crack theory and that in our case bedding could be considered as original cracks that lead to macroscopic deformation.

The strain rate also plays an important role in the plastic deformation involved and the amount of mineral reorientation that can take place. This might have implications on principal stress orientation relatively to faults planes and thus on their strength. Nevertheless, the time dependence of failure in material such as shale needs to be clarified and quantified as only few failure criteria take it into account [*Haghighat and Pietruszczak*, 2015]. We also see that the lab fault for slow strain rate and high confining pressure looks like a natural one in shales.

Another observation is that although brittle failure and stress drops systematically accompanied deformation, deformation always remained aseismic. Indeed, no acoustic emissions were detected during deformation before, during, or after failure. Yet fractures were always localized, stress weakening was observed, and slip mark evidences were found on the fault plane. This confirms that shales are good lithological candidates for aseismic creep and slow slip events [*Peng and Gomberg*, 2010].

Acknowledgments

This research was funded by TOTAL in the frame of the Fluids and Faults project. We are grateful to Damien Deldicque for technical support at ENS and for all the technical help we received from IRSN and CEREGE during drilling operations. The data produced during our experiments are available from the authors upon request (please contact the corresponding author at bonnelye@geologie.ens.fr).